

Ph.D. Dissertation Proposal

CHARM BARYON LIFETIME ANALYSIS

&

PMT TEST STATION FOR THE HF CALORIMETER OF THE CMS EXPERIMENT

UGUR AKGUN

Department of Physics and Astronomy

The University of Iowa

May 7, 2001

Abstract

This proposal consists of two parts; in the first part we are proposing a plan to measure the lifetime of weakly decaying charm baryons by using the pass2 data sample of SELEX (E781) Experiment in Fermilab. In the second part we are proposing to construct computer controlled PMT (Photomultiplier Tube) Test station in U.I. CMS laboratories to test the HF Calorimeter PMTs before the installing them to the CMS detector at CERN.

Part 1: CHARM BARYON LIFETIME ANALYSIS

1.1 Introduction

There is previous theoretical work that has focused on calculation of mass, lifetime, spin and internal quantum numbers of charm hadrons, but the experimental results are very limited.

We are proposing to measure the lifetime of weakly decaying charm baryons by using the pass2 data sample of SELEX (E781) Experiment.

1.2 Review on charm baryon lifetimes

1.2.1 Theoretical results

Weak decays of hadrons depend on the fundamental parameters of the Standard Model, in particular on the KM parameters and quark masses. It is very important to have a reliable measurement on their values from data, but it is not theoretically or experimentally easy. On the lifetimes of singly charmed weakly decaying baryons B.Guberina, R.Ruckl and J.Trampetic obtained the predictions summarized in Table 1.1 (see below) using the Bag Model of the baryon wavefunction and using the Non-Relativistic Model for baryon wavefunction [1].

Charm baryon	Lifetime (Bag model)	Lifetime (NMR model)
Ξ_c^+	0.44ps	0.37ps
Λ_c^+	0.37ps	0.23ps
Ξ_c^0	0.28ps	0.15ps
Ω_c^0	0.28ps	0.14ps

Table 1.1: Theoretical predictions for lifetimes of singly charmed weakly decaying baryon lifetimes B.Guberina et al. [1].

Later Blok and Shifman [2] with a more sophisticated calculation predicted the values of Table 1.2. According to them Ω_c^0 is either the shortest or the longest living particle among the singly charmed weakly decaying baryons. The predicted lifetime hierarchy by all the theoretical studies for charm baryons is $\tau_{\Xi_c^+} > \tau_{\Lambda_c^+} > \tau_{\Xi_c^0} > \tau_{\Omega_c^0}$ but Blok and Shifman predicts a second option to this hierarchy as $\tau_{\Omega_c^0} > \tau_{\Xi_c^+} > \tau_{\Lambda_c^+} > \tau_{\Xi_c^0}$.

Charm baryon	Lifetime
Ξ_c^+	0.28ps
Λ_c^+	0.22ps
Ξ_c^0	0.10ps
Ω_c^0	0.09ps or 0.71ps

Table 1.2: Theoretical predictions for lifetimes of singly charmed weakly decaying baryon lifetimes by B.Blok and M.Shifman [2].

1.2.2 Experimental results

First experimental baryon lifetime results were available for the Λ_c^+ [3,4,5,6] and then for the Ξ_c^+ [7,8,9,10], Ξ_c^0 [11,12] and recently for the Ω_c^0 [13,14]. The most recent results were published by the E687 experiment at Fermilab. The other experiments that had significant experimental charm baryon lifetime results are NA14, NA32, NA27, WA89, WA62, E400, E691, and more data are expected from the Cern and Fermilab experiments, (i.e., E781 (SELEX), E831 (FOCUS) and CLEO). Results of the experiments are summarized in Table 1.3, Table 1.4, Table 1.5 and Table 1.6.

L_c^+ Lifetime

<i>Experiment</i>	<i>Year</i>	<i>Decay Channel</i>	<i>Events</i>	<i>Lifetime (ps)</i>
E687	1993	$\Lambda_c^+ \rightarrow p\bar{k}\pi^+$	1340	0.215
NA14	1990	$\Lambda_c^+ \rightarrow p\bar{k}\pi^+$	29	0.180
E687	1990	$\Lambda_c^+ \rightarrow p\bar{k}\pi^+$	90	0.200
NA32	1989	$\Lambda_c^+ \rightarrow p\bar{k}\pi^+$	101	0.196
E691	1988	$\Lambda_c^+ \rightarrow p\bar{k}\pi^+$	97	0.220

Table 1.3: Summary of recent experimental results on the lifetime of Λ_c^+ .

X_c^+ Lifetime

<i>Experiment</i>	<i>Year</i>	<i>Decay Channel</i>	<i>Events</i>	<i>Lifetime (ps)</i>
E687	1998	$\Xi_c^+ \rightarrow \Xi^-\pi^+\pi^+$	56	0.410
NA32	1989	$\Xi_c^+ \rightarrow \Xi^-\pi^+\pi^+$	6	0.200
E400	1987	$\Xi_c^+ \rightarrow \Lambda\bar{K}^-\pi^+\pi^+$ $\Xi_c^+ \rightarrow \Sigma\bar{K}^-\pi^+\pi^+$	102	0.400

Table 1.4: Summary of recent experimental results on the lifetime of Ξ_c^+ .

X_c^0 Lifetime

<i>Experiment</i>	<i>Year</i>	<i>Decay Channel</i>	<i>Events</i>	<i>Lifetime (ps)</i>
E687	1993	$\Xi_c^0 \rightarrow \Xi^-\pi^+$	42	0.101
NA32	1990	$\Xi_c^0 \rightarrow p\bar{K}^-\bar{K}^{*0}$	4	0.082

Table 1.5: Summary of recent experimental results on the lifetime of Ξ_c^0 .

W_c^0 Lifetime

<i>Experiment</i>	<i>Year</i>	<i>Decay Channel</i>	<i>Events</i>	<i>Lifetime (ps)</i>
E687	1995	$\Omega_c^0 \rightarrow \Sigma^+\bar{K}^-\bar{K}^-\pi^+$	25	0.089
NA32	1990	$\Omega_c^0 \rightarrow \Omega^-\pi^+\pi^+\pi^+$	86	0.055

Table 1.6: Summary of recent experimental results on the lifetime of Ω_c^0 .

1.3 Overview of SELEX Experiment

SELEX (Segmented Large x_F Baryon Spectrometer) Experiment was a multi stage spectrometer with high acceptance for forward interactions and decays. The goal of the SELEX experiment was to produce large sample of charm hadron decays containing at least one charm quark. In addition to the high statistics charm baryon analysis, Primakoff physics, hyperon radiative decays, exotic mesons and hyperon electron scattering are the other topics of interest. The data was taken during 1996-1997 with 600 GeV Σ^- , π^- and 540 GeV proton beams.

The SELEX experiment composed of five-stage spectrometers: Beam, Vertex, M1, M2 and M3. Each spectrometer except for the Vertex, contained a bending magnet and the associated particle detectors (see Fig 1.1).

1.3.1 Beam Spectrometer

The beam spectrometer consisted of the hyperon production target, the hyperon magnet, the beam particle identification detectors, beam track detectors and the scintillators used for the trigger.

800 GeV protons from the Fermilab Tevatron accelerator hit one interaction length beryllium target. The secondary particles enter a thin 7.3m long curved channel inside the 3.5T hyperon magnet that only allows the particles with high energy (600 ± 50 GeV) to go through. Particles in the hyperon beam were tagged in the 10 TRDs (Beam Transition Radiation Detectors). Each TRD has a radiator made of 200 polypropylene foils $17 \mu\text{m}$ thick three proportional chambers filled with the mixture of Xe+30% CH_4 gas to detect transition radiation [15]. A relativistic particle crossing the boundary of media with

different dielectric constants emits transition radiation photons. The probability of radiating those photons proportional to Lorentz γ -factor hence particles with the same energy but different masses produces different numbers of hits. This is how the beam particles were identified.

The position of the beam tracks in the charm targets were measured with eight planes of $20\mu\text{m}$ pitch Beam Silicon Strip Detectors (SSD) with $4\mu\text{m}$ resolution. Each SSD has 1024 strips read out by SVX chips and has $2 \times 2 \text{ cm}^2$ sensitive area. The beam tracks, which triggered the interactions were identified by four $50\mu\text{m}$ -pitch hardware scattering trigger silicon detectors (HSD) [16]. The beam track candidates were extrapolated from the Beam SSD to the HSD planes. The track that had two or more matching hits in the HSD was identified as the trigger beam track. The beam particles interacted in five targets with combined interaction length 4.3%. Target spacing was 1.5cm. The other target properties are summarized in Table 1.7.

<u>Target</u>	<u>Material</u>	<u>Thickness(mm)</u>	<u>Z(cm)</u>	<u>A</u>	<u>Density(g/cm³)</u>	<u>Int. Length(%)</u>
1	Copper	1.6	-6.13	63.5	8.96	1.06
2	Copper	1.1	-4.62	63.5	8.96	0.76
3	Diamond	2.2	-3.10	12	3.20	0.82
4	Diamond	2.2	-1.61	12	3.20	0.82
5	Diamond	2.2	-0.11	12	3.20	0.82

Table 1.7: Charm target properties.

1.3.2 Vertex spectrometer

The vertex spectrometer consisted of the charm targets and the vertex silicon. It was designed to give high resolution of interactions in the charm targets and the secondary vertices formed from the decay of charm particles (Fig 1.2).

20 SSDs downstream of the charm targets detected the secondary tracks with high spatial resolution. The first eight detectors, called 5-cm detectors, have $20\mu\text{m}$ pitch and $5.1 \times 5.0\text{ cm}^2$ active area. The downstream 12 detectors, called mosaic detectors, have $25\mu\text{m}$ pitch and $8.3 \times 9.6\text{ cm}^2$ active area. The detectors were mounted on special granite optical bench.

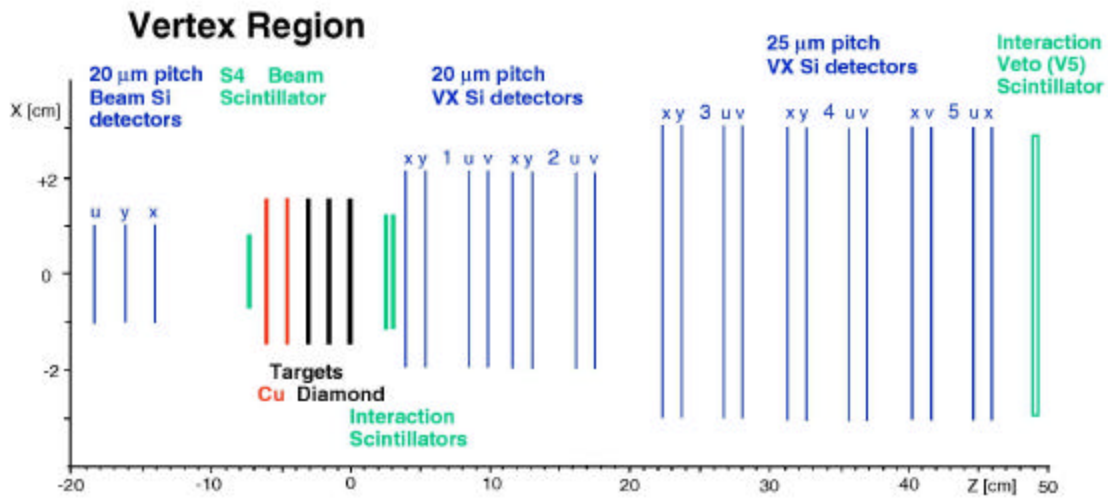


Fig 1.2: Schematic view of SELEX vertex region.

1.3.3 M1 spectrometer

The M1 spectrometer consisted of the M1 magnet and the detectors between the magnets M1 and M2 (Fig 1.3). The M1 spectrometer was designed to analyze particles in the 2.5-15 GeV/c momentum range.

The M1 spectrometer had three chambers with 3mm wire spacing and about 2x2 m² active area. Each chamber has four sensitive planes in four projections and hit detection efficiency is 90% with 0.9mm spatial resolution. There are two drift chambers, each with 2 sensitive planes measuring the hits. The drift chambers have 2.4x1.7 m² acceptance, they have 0.7mm resolution with 80% efficiency [17].

In M1 spectrometer there were three stations of Large Area Silicon Detectors (LASD) located at the end plates of M1 and M2 magnets. Three Lead Glass Electromagnetic Calorimeters were positioned at the end of M1, M2 and M3 spectrometers [18]. Each calorimeter has a hole in the middle to allow the beam and high-energy particles through. Lead glass has a density of 4.1g/cm³ and radiation length 2.5 cm and its radiation hardness was the reason to choose it as absorber.

1.3.4 M2 spectrometer

The M2 spectrometer was designed to identify and track the particles with momentum greater than 15GeV/c. The M2 spectrometer is the M2 magnet and all the detectors between M2 and M3 magnets (Fig 1.3).

There were seven Multiwire Proportional Chambers (PWC) with 2mm wire spacing in the M2 spectrometer. The three upstream PWCs have a 60x60 cm² aperture. The four downstream PWCs have a 60x100 cm² aperture. The chambers have 0.6 mm

spatial resolution with 95% hit detection efficiency [19]. To identify the electrons in M2 spectrometer 6 Electron Transition Radiation Detectors (ETRD) were used.

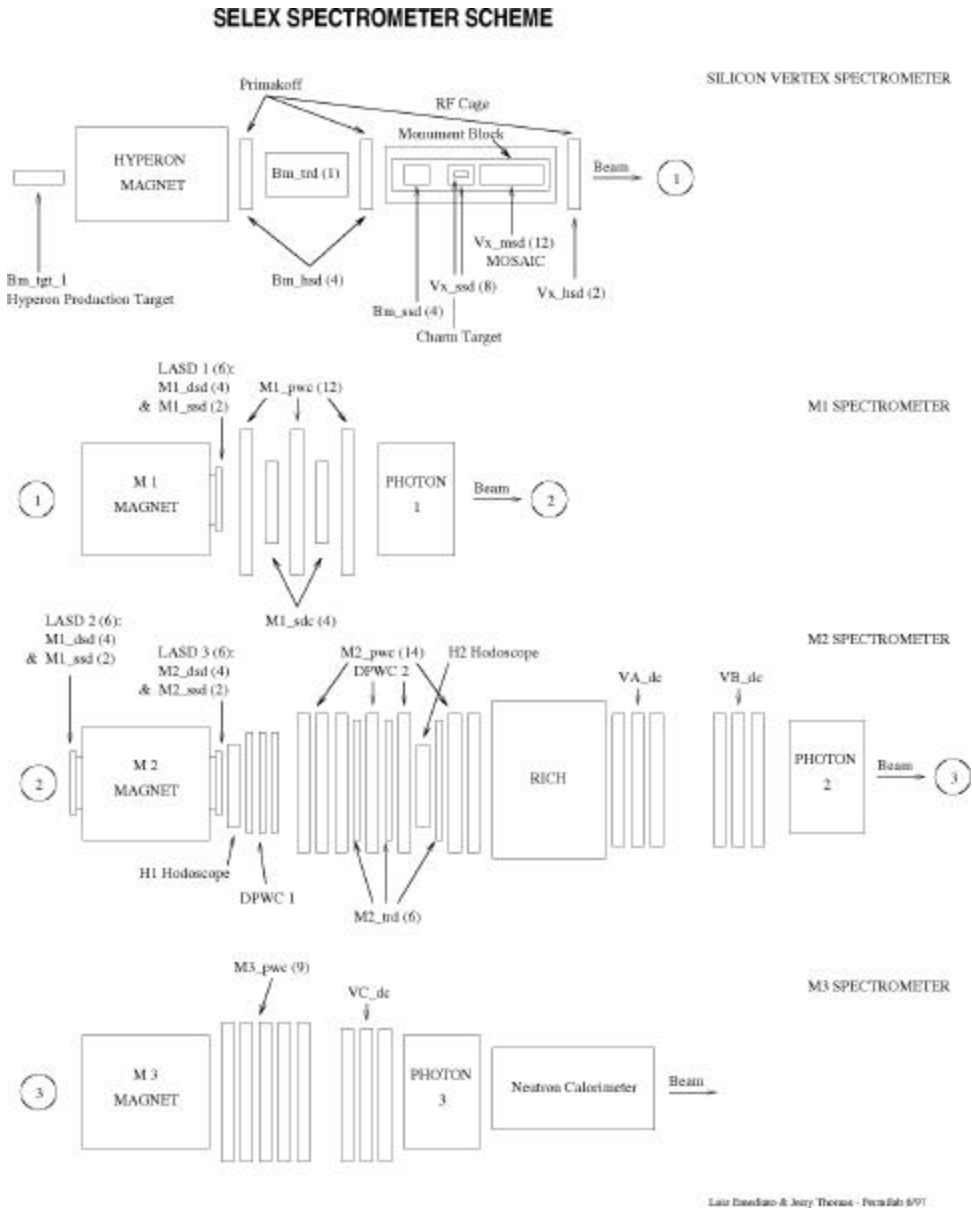


Fig 1.3: The Layouts of the SELEX Spectrometers.

The major particle identification device in SELEX apparatus was the RICH (Ring Imaging Cherenkov Counter) detector. The particles passed through 10m. long vessel filled with Ne gas emitting cherenkov light along the way. The cherenkov light was reflected on the spherical mirrors with 20m curvature. Reflected light was focused on 2848 phototube array forming rings on its surface.

1.3.5 M3 spectrometer

The M3 (see Fig 1.3) spectrometer was the place that the momentums of decay products of long-ranged hyperons were measured. M3 spectrometer consisted of a magnet with 1.3 T field strength, two MWPCs, a vector drift chamber, a lead glass electromagnetic calorimeter and a neutron calorimeter.

The last detector in SELEX apparatus was the neutron calorimeter (NCAL). It was designed to distinguish between beam particles and decay product neutrons. The NCAL consisted of 50 scintillator planes sandwiched between 50 iron sheets and 17 PWCs.

1.4 Event Selection Criteria

So as to be able to do precise measurement we need maximum efficiency on our individual event selection. For maximizing the efficiency we should find a way to suppress the background by losing the least amount of signal. There are explicit cut that we are proposing to use:

1.4.1 Vertex separation cut L/s_L

L is the distance between the primary and the secondary vertices (Fig 1.4), since the angles are very small ($\sim 10\text{mrad}$) $L = z_{\text{sec}} - z_{\text{pri}}$ is an excellent approximation. The secondary vertex position is defined by the fit of the secondary vertex tracks to the common vertex. The primary vertex is defined by the fit of the tracks from primary vertex z_{vtx} . The definition of σ_L is:

$$\sigma_L = (\sigma_{\text{prim}}^2 + \sigma_{\text{sec}}^2)^{1/2}$$

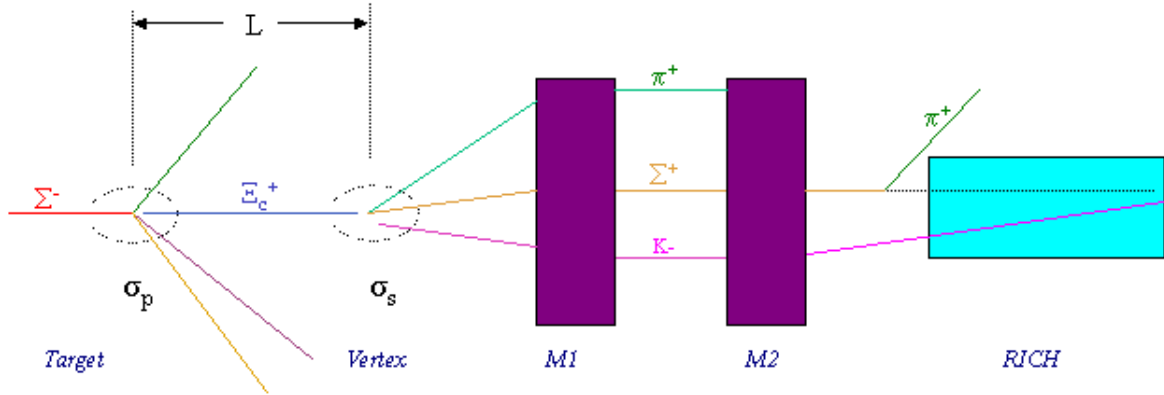


Fig 1.4: Charm event topology and selection in SELEX.

1.4.2 Charm track points back to primary vertex, p_{vtx}

The charm track is constructed as the vector sum of its secondary tracks. This track was extrapolated back to the primary vertex z_{prim} and the impact parameter with respect to the primary vertex was calculated. The pointback value, **p_{vtx}** , is the impact parameter divided by its error.

Other than those two most powerful cuts we have second largest miss-distance significance cut, target cut, soft pion cut that we can use to reduce the background and increase the event efficiency in our analysis.

1.5 Major improvements in pass2

For the charm baryon analysis particle identification is crucial. In pass2 data SELEX collaboration had some improvements to increase the efficiency of the detector. One major improvement was to increase the number of particles identified by RICH. The RICH detector is now able to identify Ω^+ , Ω^- , Ξ^+ , Ξ^- , Σ^+ , Σ^- other than electron, muon, kaon, pion and proton that could be identified in pass1 already. The RICH particle identification plots for positive and negatively charged particles in Fig 1.5 and Fig 1.6 respectively.

The charged particle reconstruction can be summarized as the successful combination of tracking, vertexing, and particle identification. The improvements in RICH covers particle identification part, but so as to increase the heavy charm baryon efficiency of the detector SELEX collaboration improved the tracking ability by adding new reconstruction software packages for the kink-by-disappearance (Fig 1.4). Kink-by-disappearance can be defined as the hyperon partial reconstruction in the cases that there is M1 vertex track but no M2 vertex track, z_{kink} is between 5m and 12m, and the particle momentum is higher than 40 Gev/c.

With those two major improvements we will have much more statistics for the heavy charm baryons.

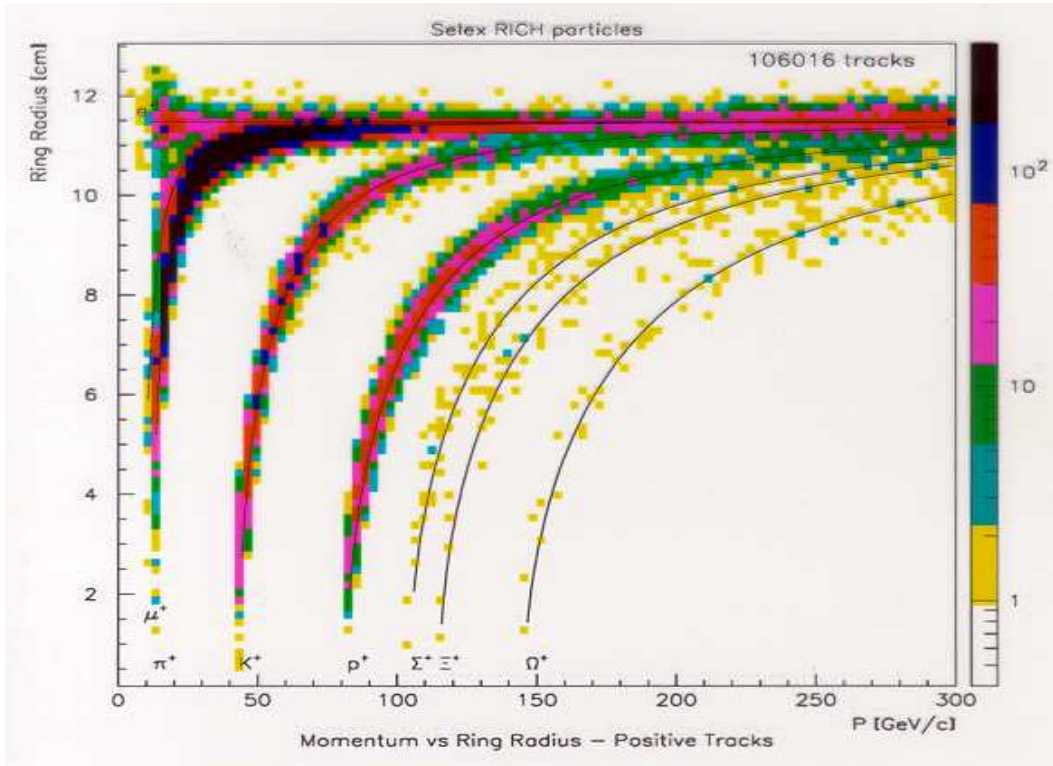


Fig 1.5: RICH particle identification plot for positively charged particles in pass2.

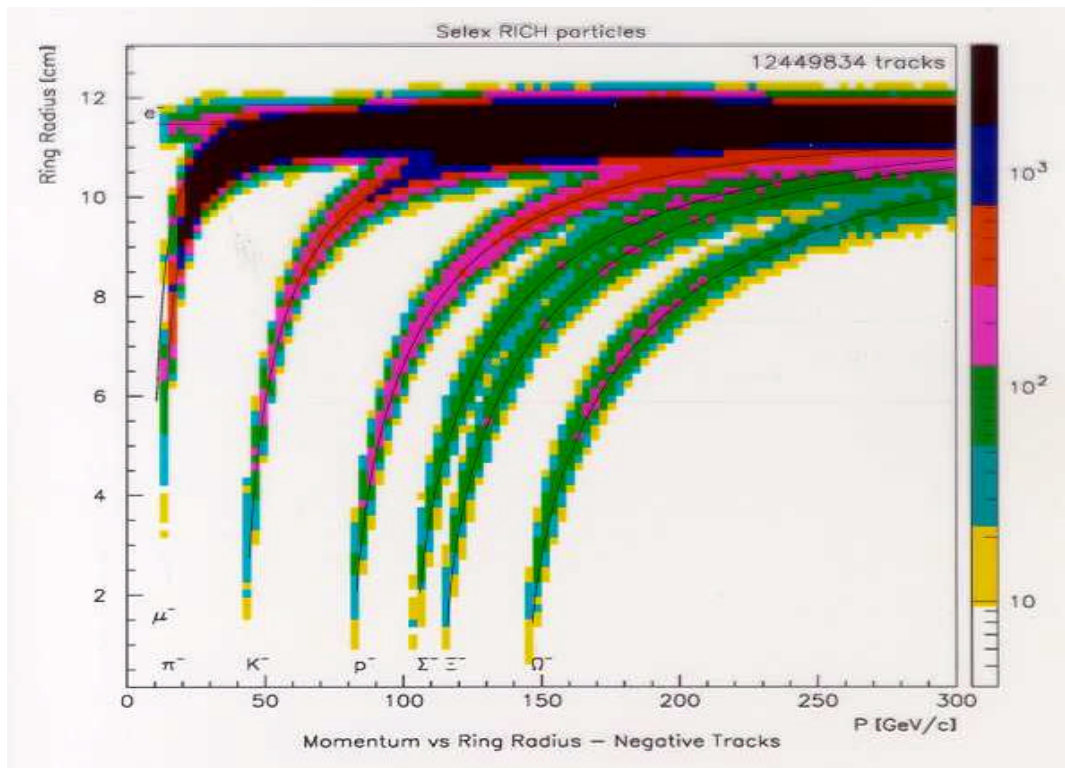


Fig 1.6: RICH particle identification plot for negatively charged particles in pass2.

1.6 Data simulation

Pass2 data for SELEX is scheduled to be available completely at the end of August 2001. Before the analysis of real data we produced the events for some of the decay channels of our interest. The event generator used was the QQ package produced by CLEO collaboration [20]. Then the generated, “perfect” events were mixed with background of SELEX data by using SOAP (SELEX Off-line Analysis Program). Data simulation is a very important tool for understanding the efficiency of our detector, for verification of the analysis techniques used and the cut optimizations for the decay channels that we are proposing to analyze.

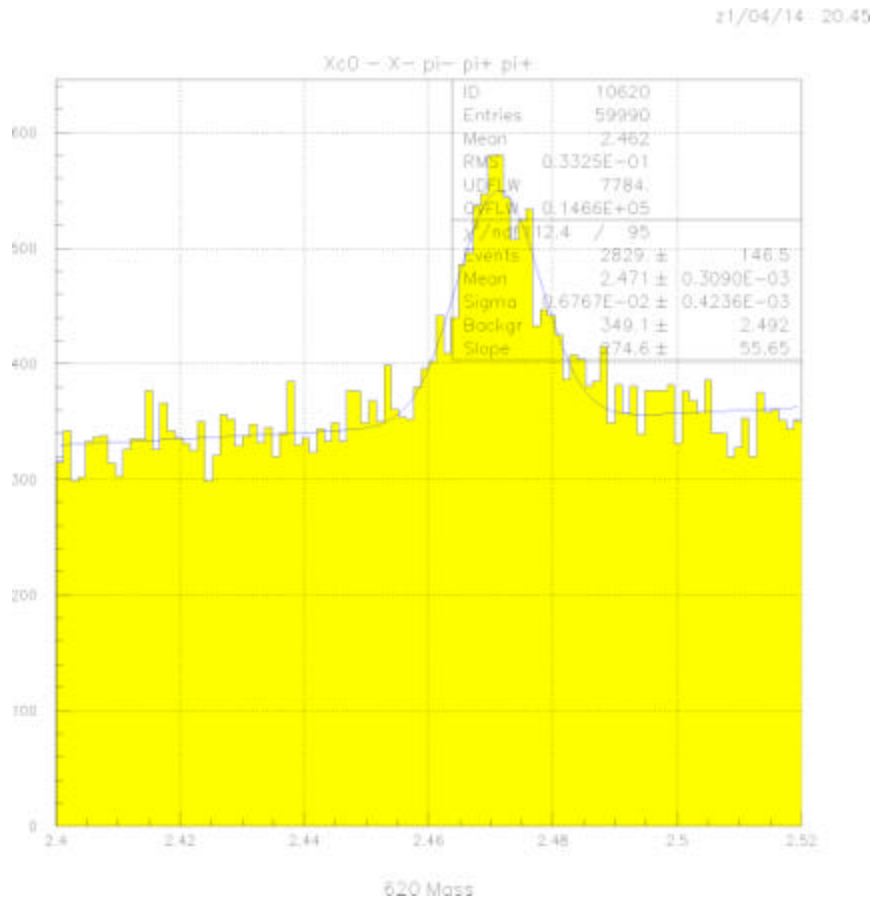


Fig 1.7: Mass distribution for the decay channel $\Xi_c^0 \rightarrow \Xi^- \pi^- \pi^+ \pi^+$.

The charm baryons that we are primarily planning to study are Ξ_c^+ and Ξ_c^0 ; Moreover, we generated and embedded the events for some of the decay channels of them. For the decay $\Xi_c^0 \rightarrow \Xi^- \pi^- \pi^+ \pi^+$ (decay ID 620) we generated 100,000 events. From the mass plot after embedding (Fig 1.7) it can easily be seen that there is huge amount of background that we need to eliminate by using the cuts on the variables of the events (Fig 1.8). The most powerful cut that we can use is vertex separation cut (L/σ_L). In the Fig 1.9, one can easily see how powerful tool the L/σ_L cut is. In the Fig 1.9, we showed the signal background variation for different L/σ_L cut values by keeping all the other variables fixed. The mass plots for different pvtx cuts are given in Fig 1.10.

The other channels that we studied explicitly so far by simulated data can be summarized as: Decay ID 602, $\Xi_c^0 \rightarrow \Xi^- \pi^+$; we generated 100,000 events, mass plot is given in Fig1.11. Decay ID 510, $\Xi_c^+ \rightarrow \Lambda^0 K^- \pi^+ \pi^+$; we generated 100,000 events, mass plot is given in Fig 1.12.

Decay ID 552, $\Xi_c^+ \rightarrow \Sigma^+ K^- \pi^+$ with $\Sigma^+ \rightarrow n^0 \pi^+$ we generated 130,000 events, mass plot is given in Fig 1.13. We studied the same decay with secondary particle Σ^+ decays into p^+ and π^0 ($\Sigma^+ \rightarrow p^+ \pi^0$), mass plot for this specific case is given in Fig 1.14. By comparing the Fig 1.13 and Fig 1.14 one can see the difference on the decays with same decay ID but different secondary particle decays.

The last decay channel that we studied by monte carlo simulation is decay ID 520, $\Xi_c^+ \rightarrow \Xi^- \pi^+ \pi^+$. We generated 130,00 events and the mass distribution is given in Fig 1.15.

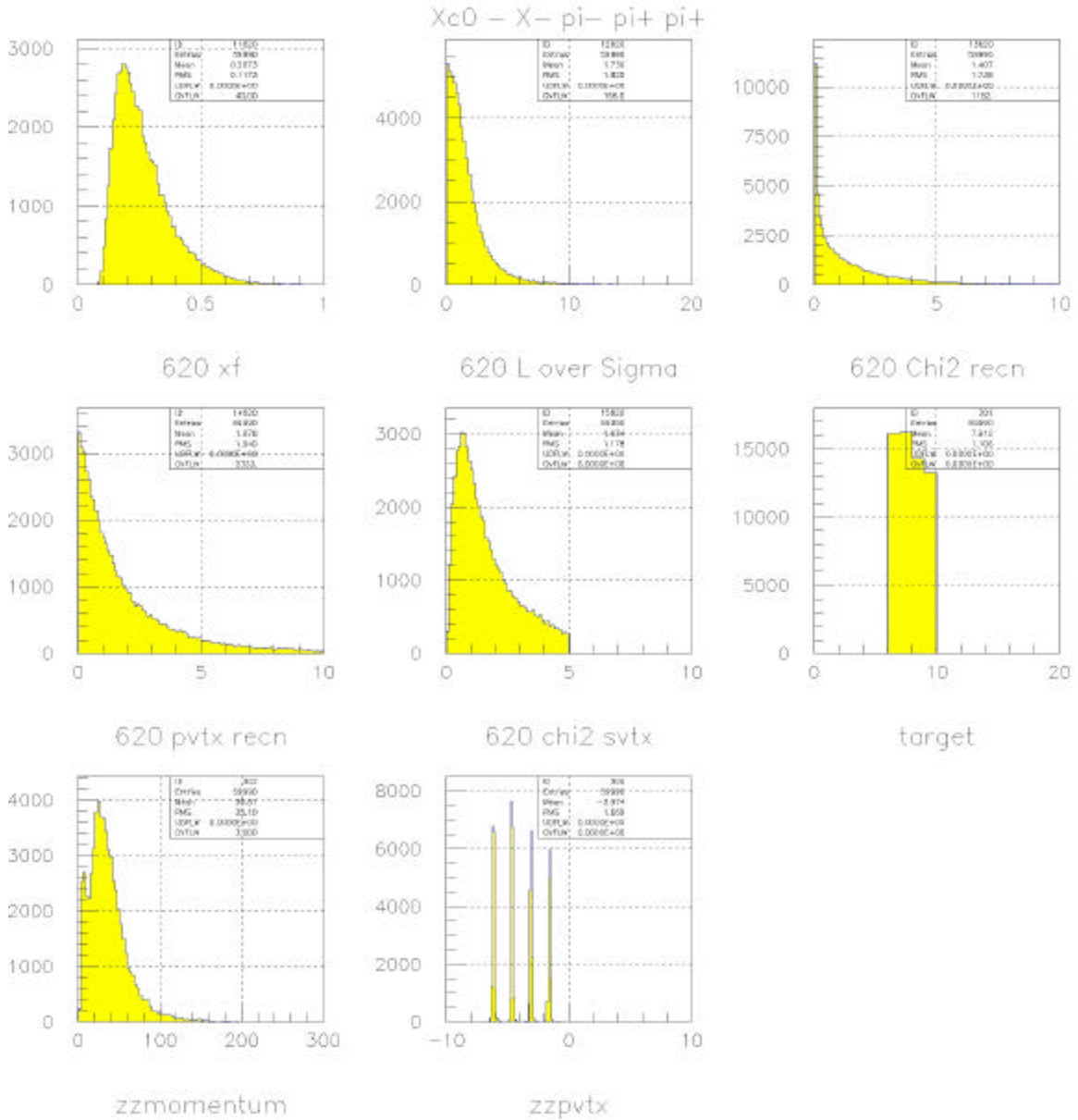


Fig 1.8: X_f , L/σ_L , pvtX, κ^2 primary and secondary, target, z-momentum in primary vertex, and primary vertex locations for the embedded events of decay channel



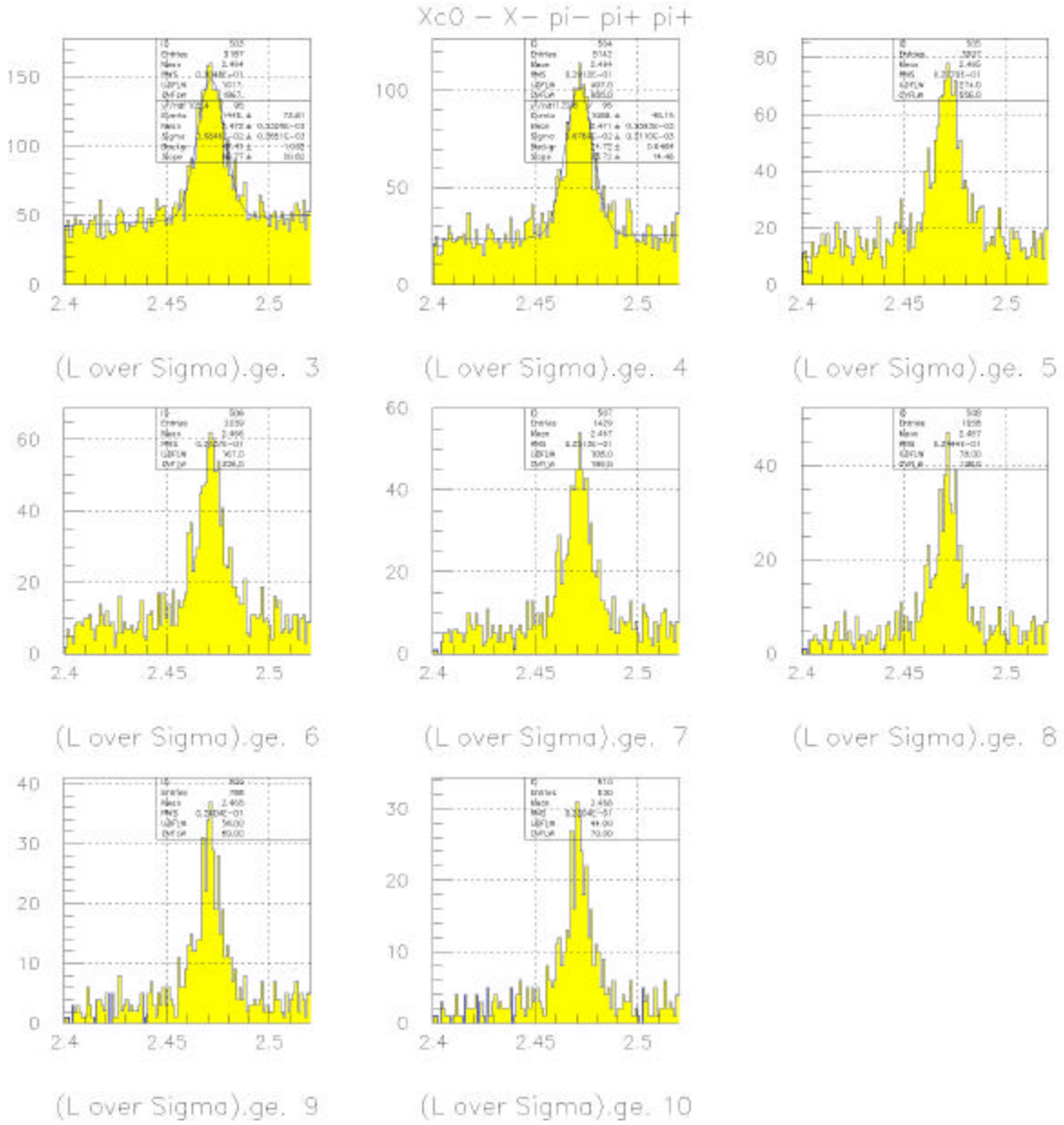


Fig 1.9: Mass plot of decay channel $\Xi_c^0 \rightarrow \Xi^- \pi^- \pi^+ \pi^+$ with different L/σ_L cuts.

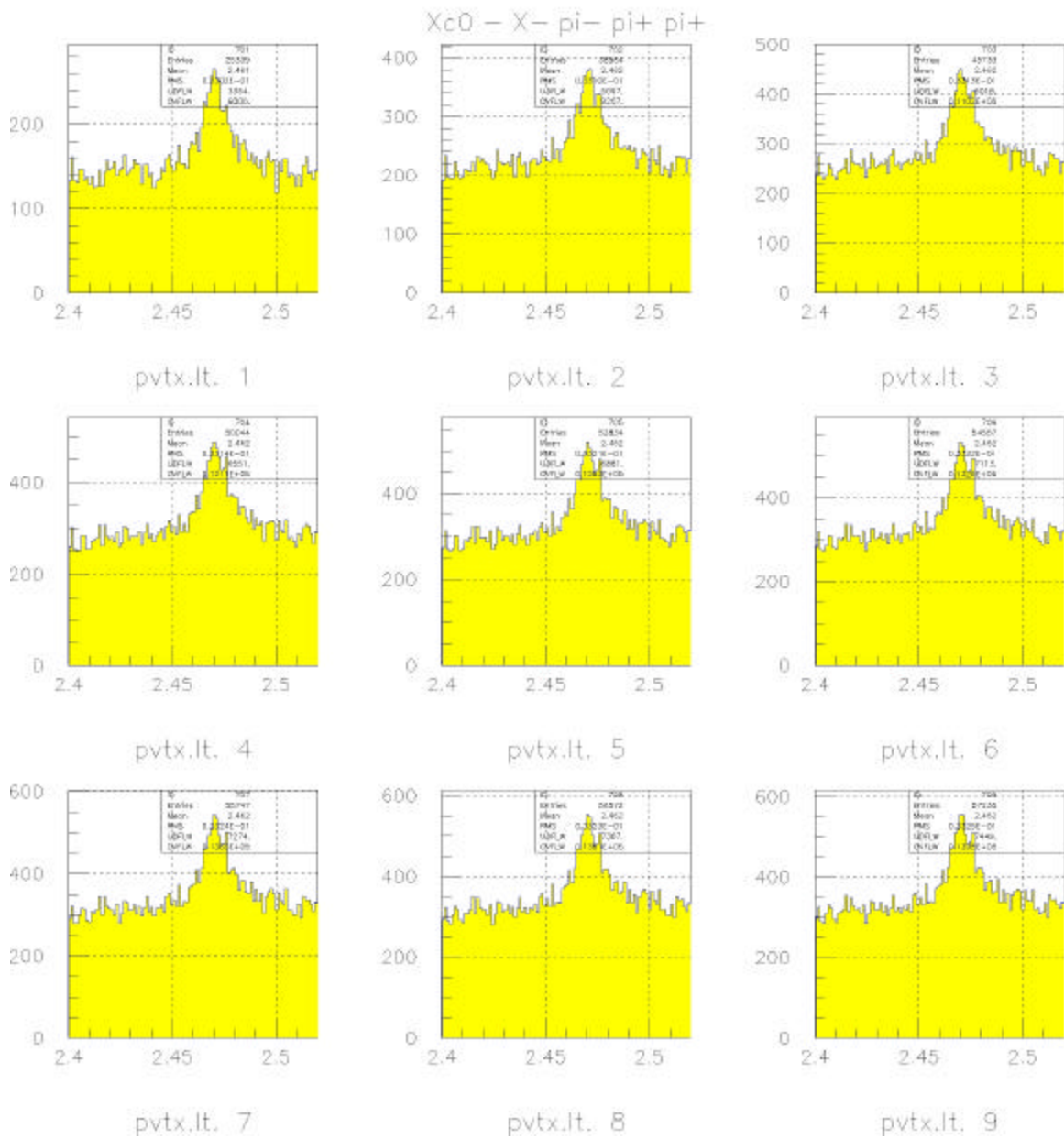


Fig 1.10: The mass plot of decay channel $\Xi_c^0 \rightarrow \Xi^- \pi^+ \pi^+$ for different pvtX cuts.

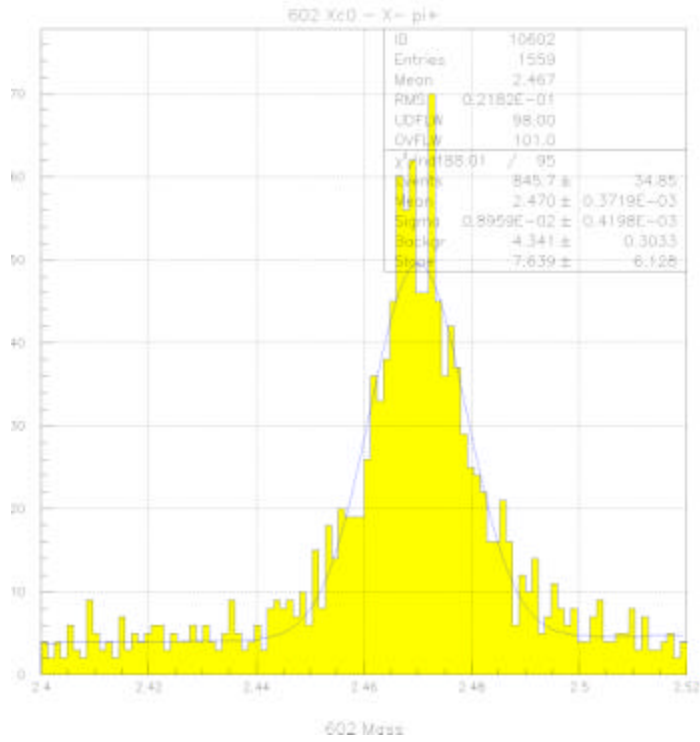


Fig 1.11: Mass distribution for the embedded events of decay channel $\Xi_c^0 \rightarrow \Xi^- \pi^+$

21/04/14 19:52

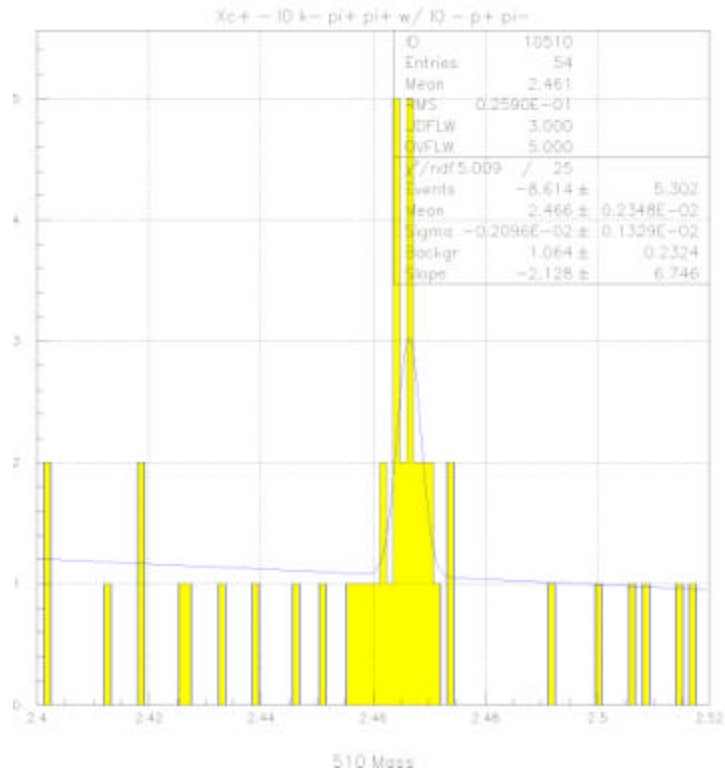


Fig 1.12: Mass distribution for the embedded events of decay channel $\Xi_c^+ \rightarrow \Lambda^0 K^- \pi^+ \pi^+$

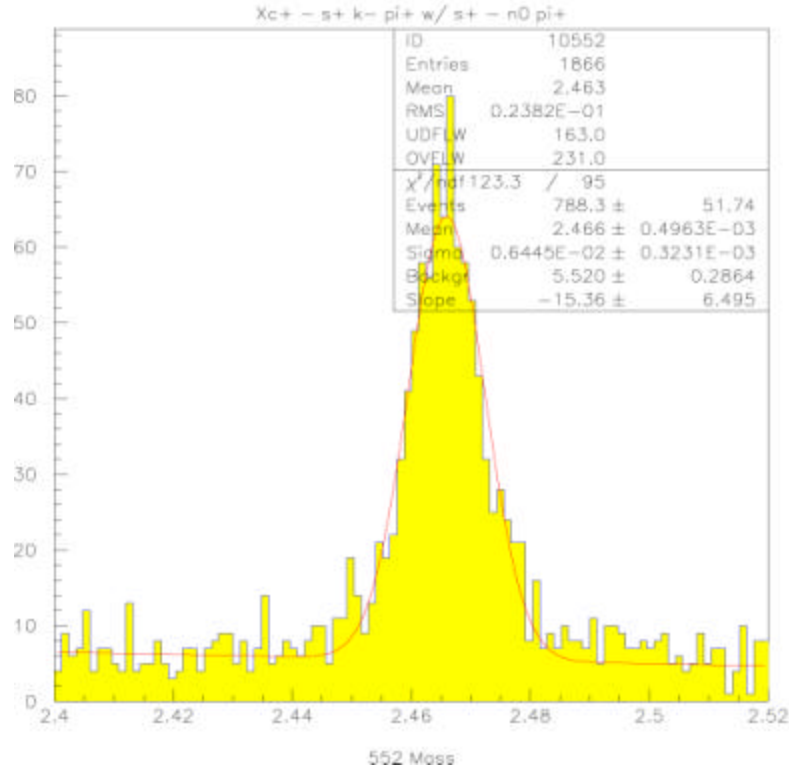


Fig 1.13: The mass distribution for the embedded events of the decay channel $\Xi_c^+ \rightarrow \Sigma^+ K^- \pi^+$ with $\Sigma^+ \rightarrow n^0 \pi^+$

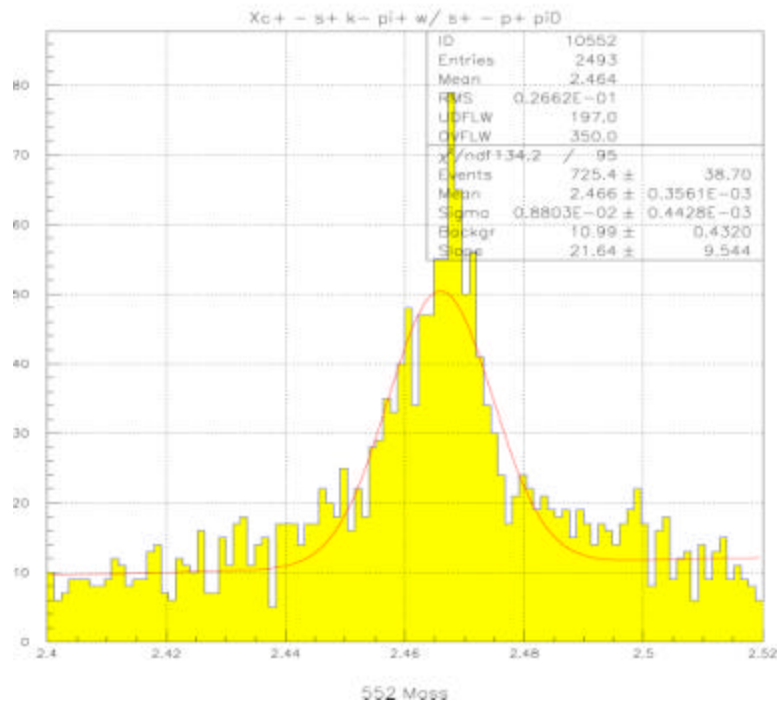


Fig 1.14: Mass distribution for the embedded events of the decay channel $\Xi_c^+ \rightarrow \Sigma^+ K^- \pi^+$ with $\Sigma^+ \rightarrow p^+ \pi^0$

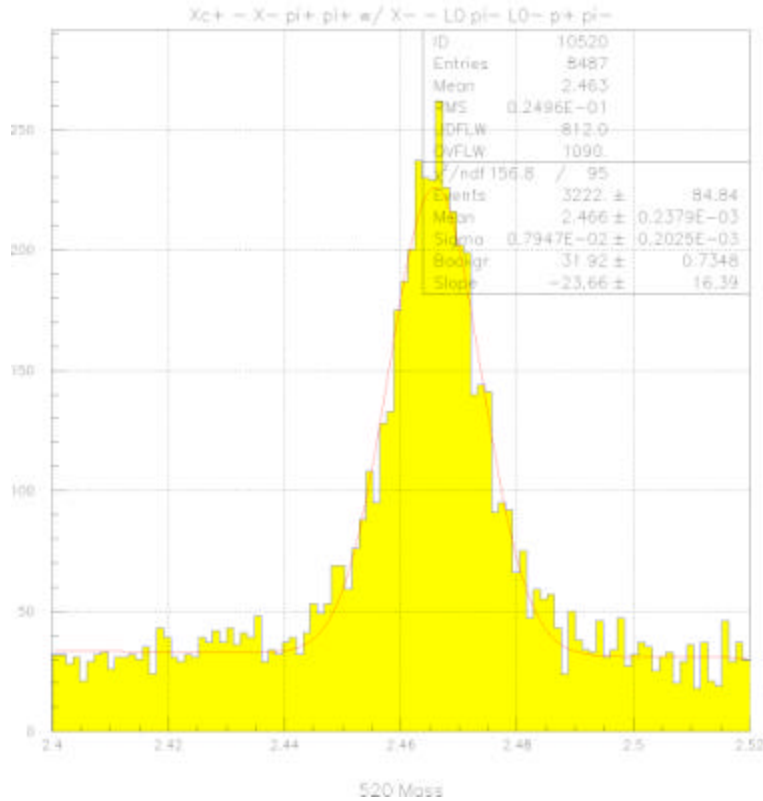


Fig 1.15: Mass distribution for the embedded events of the decay channel $\Xi_c^+ \rightarrow \Xi^- \pi^+ \pi^+$

1.7 Conclusion

The pass2 data production in SELEX experiment aims to increase the statistics of weakly decaying charm baryons. With the improvements on RICH, the particle identification ability of the detector is extended drastically. Addition of new reconstruction software packages and the improvements that have been done on the old ones will increase the statistics of the short lived charm baryons.

In conclusion, we believe that pass2 data of SELEX experiment is going to be able to produce competitive results with the previous charm hadron experiments; we also propose to make lifetime precision measurements on weakly decaying charm baryons especially for Ξ_c^+ , Ξ_c^0 and Ξ_c^- which has not been measured yet.

Part 2: PMT TEST STATION FOR THE HF CALORIMETER OF THE CMS EXPERIMENT

2.1 Introduction

The University of Iowa is one of the institutes that participate in CMS experiment of LHC project at CERN (European Organization for Nuclear Research), in Geneva, Switzerland. One component of the US-CMS construction project is a forward hadron calorimeter (HF). Part of this calorimeter will be the procurement of 2700 PMTs (Photomultiplier Tubes) to read out the calorimeter fiber.

We are proposing to construct computer controlled PMT Test station in U.I. CMS laboratory to test those 2700 PMTs before the installation to the main detector.

2.2 CMS Overview

2.2.1 Physics Performance

The CMS detector has been designed to detect cleanly the diverse signatures from new physics by identifying and precisely measuring muons, electrons and photons over a large energy range and at high luminosity. It is also aimed to take advantage of the expected lower luminosity running in the early years of the LHC [21].

Studies have been made of the performance of CMS in detection and measurement of various physics signals from proton-proton and heavy ion collisions. The wide range of physics interests of CMS can be summarized as: Searches for the

Standard Model (SM) Higgs boson and the various Minimum Supersymmetric Standard Model (MSSM) Higgs bosons, gluino, squark searches, CP-violation measurements in the B sector, observation of B_s^0 oscillations, and possible signals for QCD deconfinement via the relative suppression within the γ family in heavy ion collisions, top physics, searches for the new heavy gauge bosons and resonant strong interaction spontaneous symmetry-breaking models.

2.2.2 CMS Detector

The CMS detector (Fig 2.1) has a length of 21.6 m (very forward calorimeters excluded), a diameter of 14.6 m and a total weight of 14500 tons. There are four main subsystems of the detector; magnet, muon system, tracking and calorimetry.

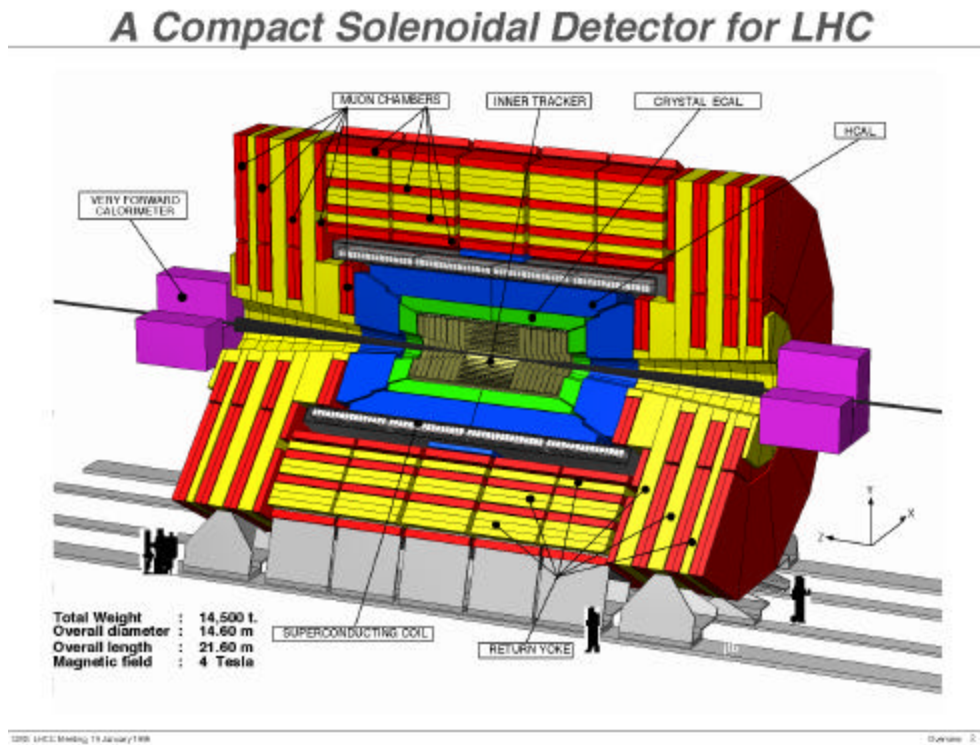


Fig 2.1: Three-dimensional view of the CMS Detector.

a) *The Magnet*

The magnet of the CMS detector (see Fig 2.1) is a long superconducting solenoid of length 13 m and inner diameter 5.9 m and it creates a uniform magnetic field of 4 T. The magnetic flux is returned via a 1.8 m thick saturated iron yoke which is instrumented with muon stations. The favorable aspect of the ratio of the solenoid allows efficient muon detection and measurement up to a rapidity of 2.4 without the need of forward toroids. Thus the muon spectrometer uses single magnet, simplifying the detector design. The inner coil diameter is large enough to accommodate the tracker and the calorimeters. Since the magnet is the main element of CMS in terms of size, weight, and structural rigidity, it is used as the principal structural element to support all other barrel detector components [21].

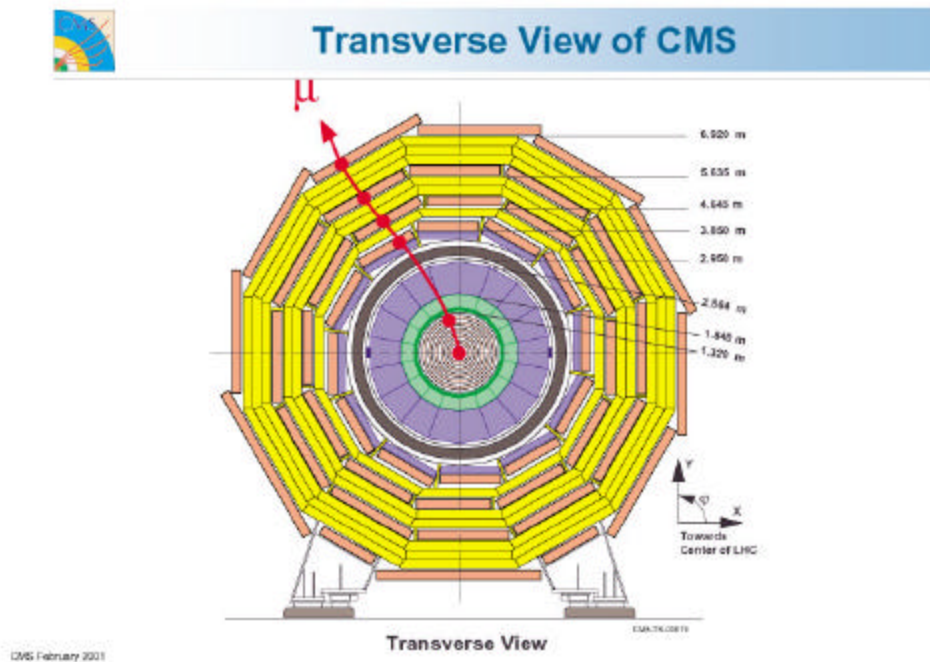


Fig 2.2: Transverse view of the CMS detector.

b) *The Muon System*

In CMS detector a muon sees four muon stations over most of the solid angle (see Fig. 2.2). Each of the four barrel stations (MS1 to MS4) consists of twelve planes of aluminum drift tubes (DTs), arranged in twelve azimuthal sectors, such that there are no cracks pointing to the primary vertex (see Fig. 2.2). The endcap muon system also consists of four muon stations MF1 to MF4. Each station consists of sectors of CSCs overlapping in azimuth to maintain full coverage. The two stations MF1A and MF1B have been added to ensure that all muon tracks transverse four station at all rapidities, including the transition region between the barrel and the endcaps ($1 < |\eta| < 1.5$) (Fig. 2.3).

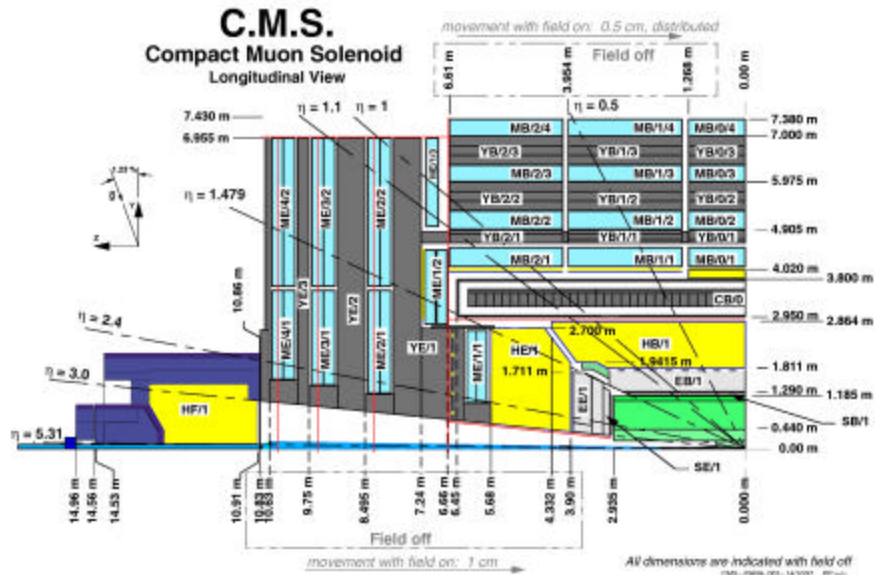


Fig 2.3: Longitudinal view of the CMS detector.

Efficient muon detection is guaranteed up to $|\eta| = 2.4$ for $P_t > 4$ GeV. The acceptance of the hadronic endcap HF has been extended up to $|\eta| = 3$ to allow the insertion of a thicker conical iron structure. This cone significantly reduces the background rate in the four forward stations (MF1 to MF4). It can also support the endcap calorimeters (HF and EF) without cutting into the azimuthal acceptance [21].

c) Tracking

The design and the goal of the tracking system is to reconstruct the isolated high P_t tracks with an efficiency of better than 95%, and high P_t track within jets with an efficiency of better than 90% over the rapidity range $|\eta| < 2.6$.

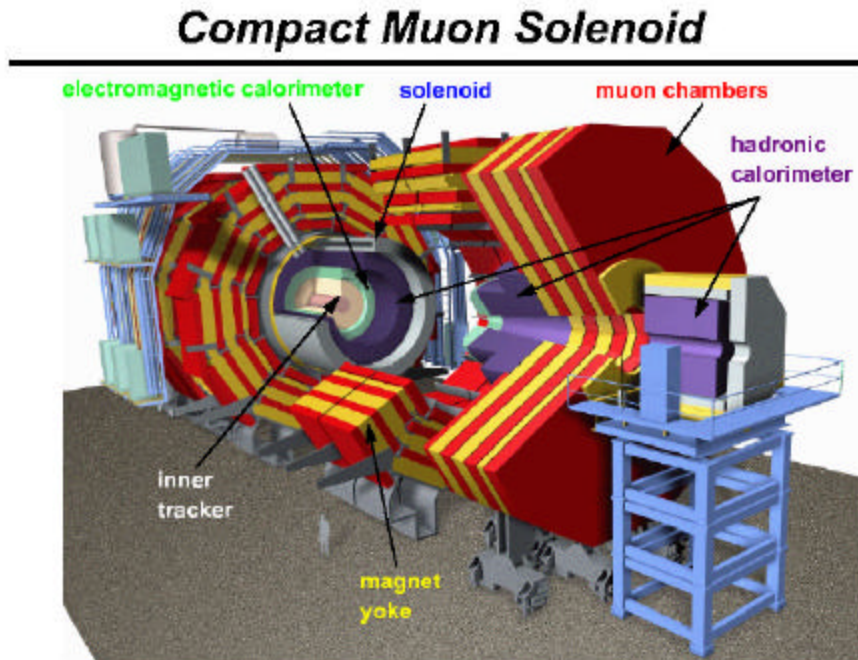


Fig 2.4: Another three-dimensional view of CMS detector.

The momentum resolution required for isolated charged leptons in the central rapidity region is $\Delta p_t/p_t \cong 0.1 p_t$ (p_t in TeV). This will allow the measurement of the lepton charge up to $p_t \cong 2$ TeV. This will also allow frequent in situ calibration of every cell of the crystal electromagnetic calorimeter, needed to maintain the high-energy resolution of the calorimeter, using the high rate of precisely measured electrons from W and Z decays. The silicon pixel detectors close to the interaction vertex is designed to give 20 μm resolution in the transverse plane and 100 μm in the z direction. The solid-state pixel and microstrip detectors and gas microstrip detectors will provide the granularity and precision on pattern recognition at high luminosities [21].

d) Calorimetry

The high resolution PbWO₄ (Lead Tungstate Crystals) Electromagnetic calorimeter (ECAL) (Fig 2.4) is designed to measure the energies of electrons and photon with high precision. The physics channel that imposes the strictest performance requirement for the ECAL is the decay of the Higgs boson with mass in the range 100-140 GeV into two photons. All the terms making up the energy resolution have to be kept small and should be roughly equal at photon energies corresponding to half the Higgs mass.

The hadron calorimeter (HCAL) surrounds the ECAL (see Fig 2.4) and acts in conjunction with it to measure the energies and directions of particle jets, and to provide hermetic coverage for measuring missing transverse energy. The pseudorapidity range of $|\eta| < 3.0$ is covered by the barrel and the endcap HCALs which sit inside the 4 T field of the CMS solenoid [21].

2.3 *The Very Forward Calorimeter Overview*

There are two very forward calorimeters (VFCAL) in CMS detector and they cover the pseudorapidity range from 3.0 to 5.0. The VFCALs are located at 11m away from the interaction point as shown in Fig 2.4. VFCAL improves the measurement of the missing transverse energy and enables very forward jets to be identified and reconstructed. These jets are distinguishing characteristic of several important physics processes; in the case of heavy Higgs production, they materialize through WW and ZZ fusion. In the case of slepton, chargino and neutralino searches, they are background signatures.

The Large Hadron Collider will be operating at a luminosity of $10^{34} \text{ cm}^{-2} \text{ sec}^{-1}$ the average particle multiplicity at the IP per crossing is about 5700 with an RMS value of 1200. This corresponds to a rate of $2.3 \times 10^{11} \text{ sec}^{-1}$, equivalent to 280 particles/crossing/rapidity unit. $4.5 < |\eta| < 5$ region will experience a flux of about $6.0 \times 10^6 \text{ cm}^{-2} \text{ sec}^{-1}$ and absorbed doses will reach about 100 Mrad/year. Therefore, the detectors must be able to survive in an exceptionally high radiation field. The CMS experiment has chosen the quartz fibers as the active material for the very forward regions because the high-purity quartz is known as very radiation-hard [22].

A calorimeter with optical quartz fibers embedded into an absorber matrix was proposed by HCAL group [23] for producing extremely fast signal as well as radiation hardness. A lot of simulation and test beam studies that have been made on quartz fiber calorimeter prototypes by CMS HCAL group, which includes University of Iowa CMS group. Those studies can be summarized as; testing the response of the prototype CMS

2.4 Photomultiplier Tubes (PMTs) in HF Calorimeter

In HF calorimeter (Fig II.V) the PMTs (photomultiplier tubes) will operate in a temperature-controlled environment, and be inside individual magnetic shields to protect them from a moderate magnetic field. Due to the large number of tubes, they must be small in diameter. The light from the calorimeter fiber will be in the 300-600 nm range. So the photocathode must have good quantum efficiency in that wavelength region. The tubes will also be in a radiation environment, and they should not appreciably deteriorate over a 10 years lifetime of operation. As in all calorimeters, a premium is placed on the short-term and long-term gain stability of the tubes as functions of time and average anode current; it is also important that the tubes have large linear dynamic range at all gains.

2.5 CMS HF PMT Specifications

The specifications for the PMTs that will be used in HF were determined by using the specifications of the tubes used in the prototype studies. Some specifications were added due to the requirements of operation in LHC environment and the HF design.

These specifications can be summarized as:

- Effective Photocathode diameter is 22 to 28 mm.
- Average Quantum efficiency > 15 % at 400-500 nm.
- Anode current vs. cathode position less than 20%.
- Photocathode lifetime > 200 mC.

- Gain 10^4 to 10^5 at less than 0.75% of $V_{KA}(\max)$.
- Single photoelectron resolution; rms/mean of single photoelectron peak 50 % or better.
- Pulse linearity; less 2% deviation from 0 for 1-3000 photoelectrons.
- Transit time less than 25 ns.
- Transit Time Spread less than 2ns.
- Anode Pulse Rise time less than 5 ns.
- Pulse width less than 15 ns.
- Gain (1/2)-lifetime greater than 1500 C.
- Average cathode current is less than 1 nA (with gain = 10^4).
- Average anode current is less than 10 μ A (with gain = 10^4).
- Anode Dark Current is less than 2nA (with gain = 10^4).
- Stability; less than 3% deviation within any 48 hours period.
- Window Material is Borosilicate glass.
- Envelope is opaque and -HV conductive coatings.
- Radiation tolerance with 10 kRad/10year, anode luminosity loss < 10%.

2.6 PMT Test Station

The PMT test station that we are proposing to construct in University of Iowa CMS laboratories will test 2700 PMTs weather they fit CMS HF calorimeter specifications or not. All measurement procedures will be automated and computer-controlled to minimize individual biases and interventions, daily test shifts will be supervised by an expert, who will also review the archived data of the day and certify

their validity. The manufacturer will provide 200 PMT per month, we are proposing to do the necessary tests on every PMT in an hour in the PMT test station.

Measurements will be performed at temperature and humidity controlled system. Previous studies [32,33] showed that humidity and temperature changes are major factors on the efficiency of the PMTs. For each delivery batch, sample measurements will be performed for temperature and magnetic field dependence too. The data for each PMT will be stored in appropriate archive files on disk and copied to permanent storage media. For each PMT an entry will be printed and logged to a general PMT directory and test logbooks. The PMT's, conforming to acceptance criteria, will be sorted in classes and stored (Storage OUT), ready for installation. Those not conforming will be returned to the manufacturer.

All measurement procedures will be automated and computer-controlled to minimize individual biases and interventions, daily test shifts will be supervised by an expert, who will also review the archived data of the day and certify their validity.

The electronic system for the Test Setup will include:

- Pulsers for the Laser, LED and calibration pulses;
- Digital control circuits for: HV and LV power supplies, laser parameters and settings, stepping motors for moving parts in Test Box, probes for temperature, humidity and magnetic field inside the Test Box, Safety circuits on door, sliding mechanics, etc
- Trigger logic for DAQ, monitors and gates
- ADC and TDC for amplitude and timing measurements
- Digital Oscilloscope for measuring and recording pulse shapes

The Test Box assembly will consists of:

- PMT holder support with position remote control;
- Optical Manifold (O. M.) providing fiber coupling to individual PMT's and receiving light from: Laser system with variable wavelength, LED system pulsed at high frequencies, radioactive sources and scintillators.
- Monitoring and control devices.

The Data Acquisition System (DAQ) will consist of:

- VAX3200 (with back plane), which is a functional DAQ system with CAMAC
- Interface cards and software of LabView for the mobile DAQ.

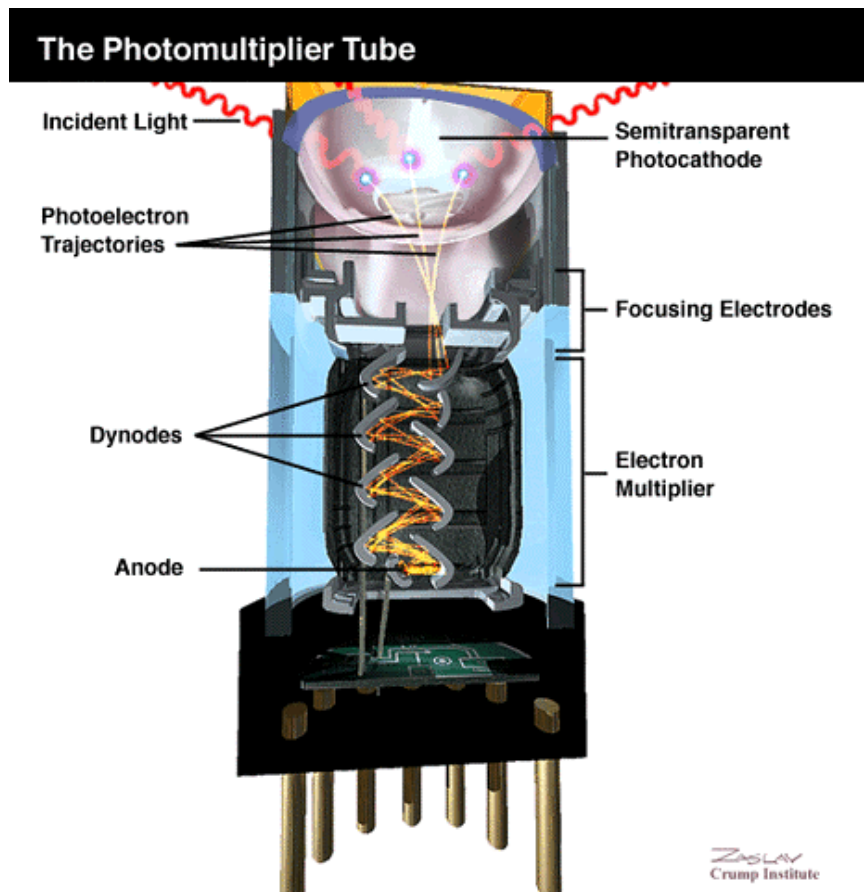


Fig. 2.6: The internal structure of a Photomultiplier Tube.

2.7 Preliminary Tests

Before constructing the computer controlled automated PMT test station, we performed some preliminary tests in our laboratory. We performed the anode dark current, timing characteristics, gain, photocathode sensitivity and linearity tests on three Hamamatsu PMTs (with serial numbers of ZC9898, ZC9957, ZC9903 and ZC9900) and two Electron Tubes PMTs (with serial numbers D843WSB and D844WSB).

2.7.1 *Anode Dark Current*

Even in total darkness, a current can still be measured at the anode of the photomultiplier tube (Fig 2.6); its causes include thermionic emission, field effects, and leakage currents. It depends particularly on the composition of the cathode, and, throughout the usual range of supply voltages, varies ideally as the gain [34].

Manufacturer's base for the Hamamatsu phototubes 7525 is designed for a negative HV and direct coupling. Therefore anode can be connected to a picoammeter directly while the pmt is in a dark box. Test sheet provided by the manufacturer includes dark current measurements (at 1500 V) for the four tubes that we have. Our dark current measurement for three of the tubes (Serial numbers ZC9900, ZC9903, ZC9898) turned out to be slightly lower than that of the manufacturer (see Fig. 2.7). We may not be doing our measurements under the same conditions as the manufacturer has done. However, these values are very low compared to the dark current specification of the CMS HF. But one pmt (serial number ZC9957) gave much higher values than the manufacturer's dark current values (see Fig. 2.8), this pmt can be an example for the ones that we will return to the manufacturer.

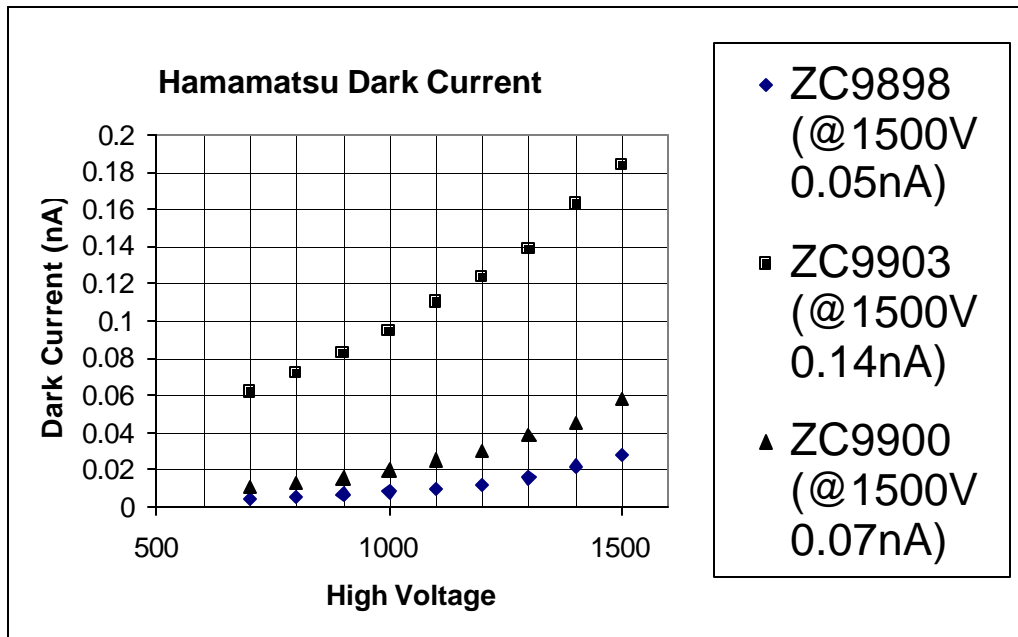


Fig. 2.7: The Dark current measurements, which are in good agreement with the manufacturer’s data, for three Hamamatsu pmts.

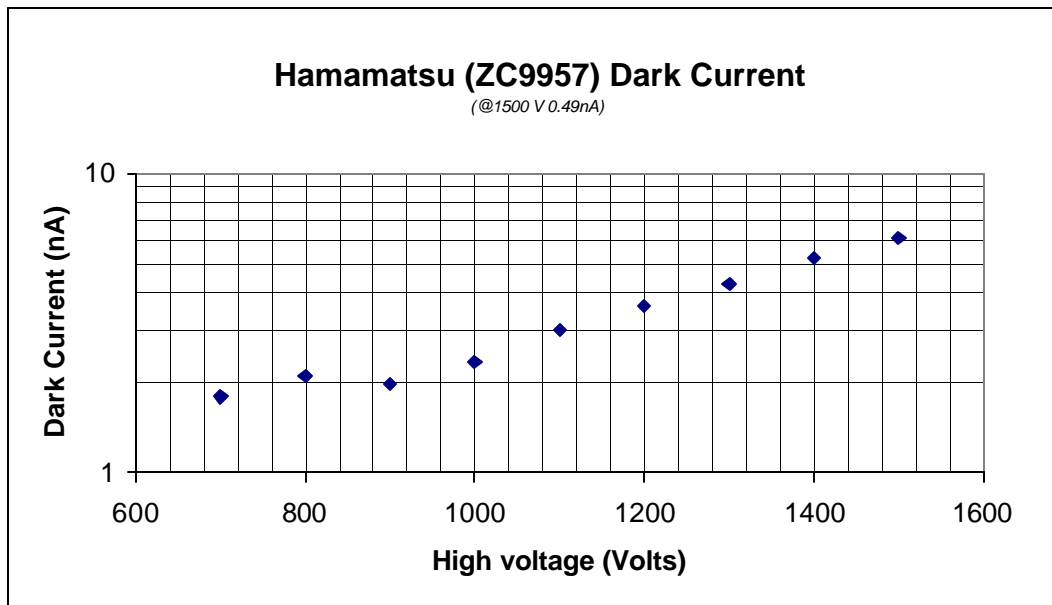


Fig. 2.8: The Dark Current measurement, which is higher than the manufacturer’s values, for one Hamamatsu pmt.

2.7.2 Timing Measurements

The photomultiplier tube is a photodetector that has an exceptionally fast time response. The time response is primarily determined by the transit time required for the photoelectrons emitted from the photocathode to reach the anode while being multiplied and also the transit time difference between each photoelectron. Accordingly, fast response photomultiplier tubes are designed to have a spherical inner window and carefully engineered electrodes so that the transit time difference in the tube can be minimized [35]. The rise time of the pulse is defined to be the time difference between 10% amplitude of the pulse and 90% amplitude of the pulse when it is increasing (Fig 2.9).

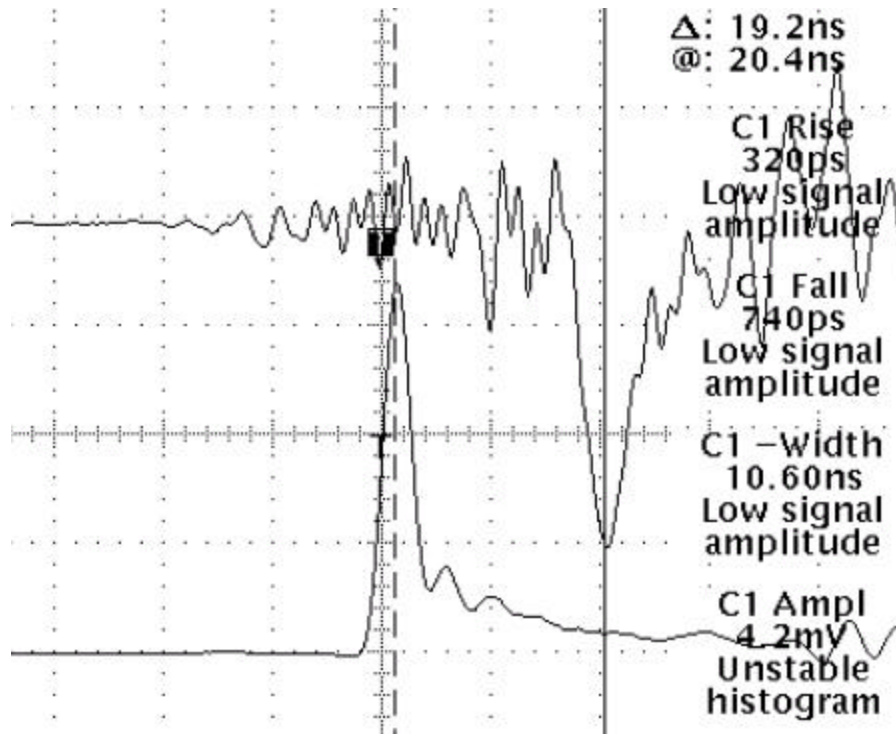


Fig 2.9: A sample signal of PIN diode, PMT system.

We used a 337 nm. Laser as a light source for the timing measurements. Laser beam was directed to the 30/70 beam splitter through a neutral density filter with factor 1. Direct beam goes into the phototube assembly and the reflected beam goes into a PIN diode. PIN diode provides a reference time for measuring the transit time and also for triggering the signal. By observing the PIN diode output in coincidence with the phototube output on a 500 MHz Tektronix digital oscilloscope, we can measure the leading edge rise time, pulse width, and transit time of the phototube. Our results agree with the typical values quoted on the specification sheet. Transit time slowly approaches to 13ns as we increase the voltage to 1500. Leading edge rise time and pulse width are almost constant with some small fluctuation. Leading edge is about 2ns. Pulse width is about 3ns. Both leading edge and pulse width measurements are in fact the characteristics of the whole setup not just the phototube. Our estimate for the leading edge rise time is around 1 ns which is in good agreement with the manufacturer specifications (Fig 2.10).

2.7.3 Collection efficiency and Current Gain:

The electron multiplier of a photomultiplier tube is designed with consideration to the electron trajectories so that electrons are efficiently multiplied at each dynode. However, some electrons may deviate from their favorable trajectories, not contributing to the multiplication. The probability that the photoelectrons may land on the effective area of the first dynode is termed the collection efficiency [35].

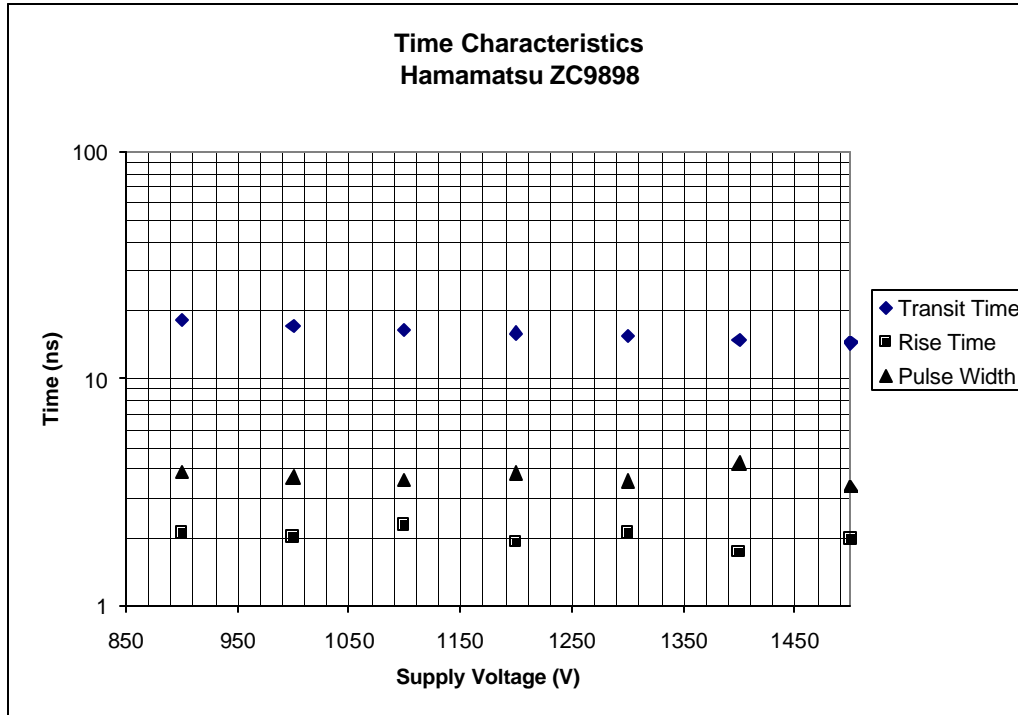


Fig 2.10: Timing characteristics of Hamamatsu pmt, serial number ZC9898.

The current gain is defined to the proportionality of the cathode current to the anode current. So as to measure the current gain we apply the voltage between the photocathode and the first dynode all the measured currents corrected by cathode dark current. Then the same dc light source (tungsten light bulb) used to illuminate the pmt when we are reading the anode current, but the light was attenuated by a factor of F (was 3 in our measurements) by using the neutral density filters. The anode current was corrected with anode dark current too. Then the current gain was calculated by using the equality: $gain = (I_C/I_A) F$

The results of gain measurements for the four Hamamatsu pmts are given in the Fig 2.1

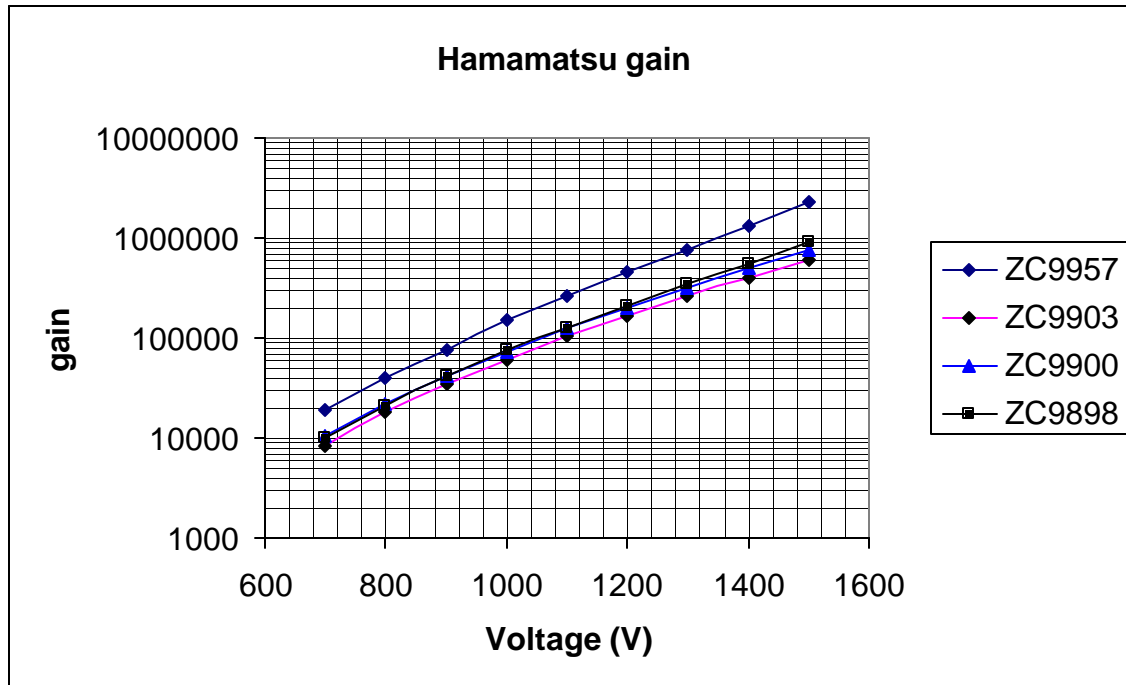


Fig 2.11: Current gain measurements for four Hamamatsu pmts.

2.7.4 Linearity

The photomultiplier tube provides good linearity in anode output current over a wide range of incident light levels including the photon counting region. In other words, it offers a wide dynamic range. However, if the incident light amount is too large, the output begins to deviate from the ideal linearity. This is primarily caused by anode linearity characteristics, but it may also be affected by cathode linearity characteristics when a photomultiplier tube with a transmission mode photocathode is operated at a low supply voltage and large current. Both cathode and anode linearity characteristics are depended only on the current value if the supply voltage is constant, while being independent of the light wavelength [35].

We measured the linearity of Hamamatsu pmts, by using different neutral density filter values. The pulse linearity plot in Fig 2.12 shows that the pmt gives linear signal in

the region of 1-3000 photoelectrons, which is in good agreement with HF pmt specifications.

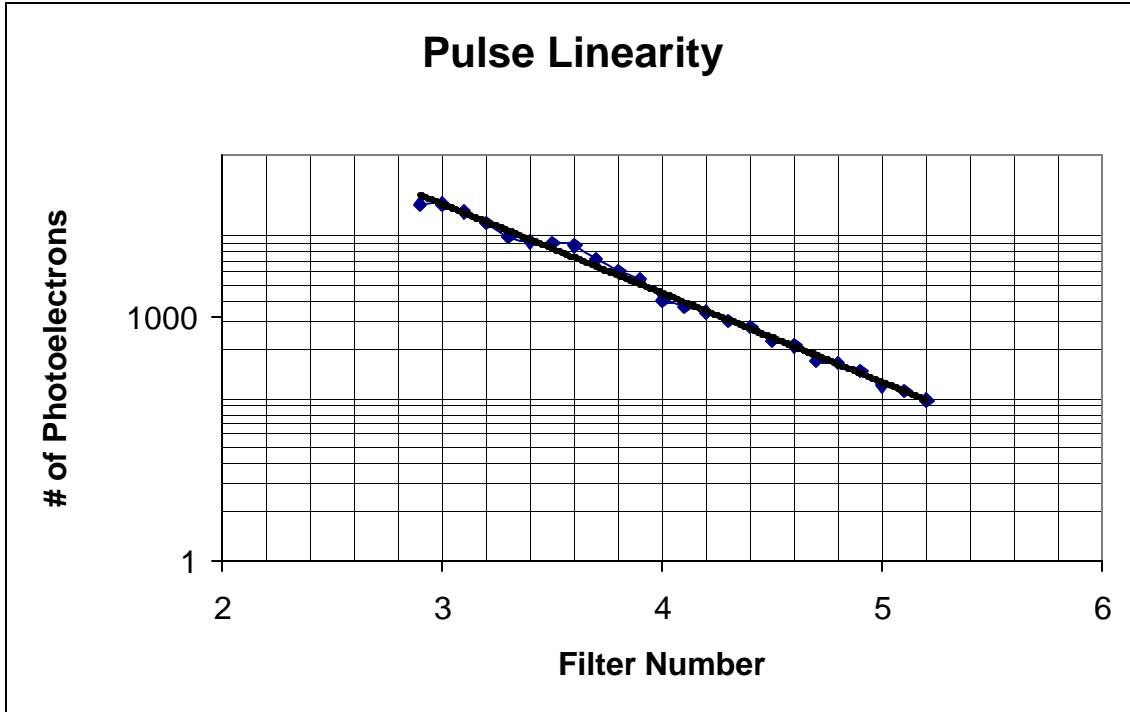


Fig 2.12: Pulse linearity measurement of Hamamatsu pmt (serial number ZC9898).

2.8.1 Conclusion

The HF calorimeter will be one of the important pieces of the CMS experiment. The previous work done by HF group cleared the questions about the absorber material and fiber types that will be used. The PMT choice will be another crucial point for the performance of the detector. Before installing 2700 PMTs to the main detector we have to be sure that every one of them fits the CMS-HF requirements. The preliminary results showed that we could perform the necessary tests with high precision. In conclusion we are proposing to construct a PMT Test Station in U.I. CMS Laboratory to test the 2700 PMTs before the installation to the main detector.

References

- [1] B.Guberina, R. Ruckl and J. Trompetic, Z. Physics C33 (1986) 297
- [2] B. Blok and M.Shifman, in Proc. Of Third Workshop on Tau-Charm Factory, Edited by J. Kirkby and R. Kirkby.
- [3] P. L. Frabetti et al., PRL 70 (1993) 1755
- [4] M. P. Alvarez et al., Z. Physics C47 (1990) 539
- [5] S. Barlog et al., PL B218 (1989) 374
- [6] J. C. Anjos et al., PRL 60 (1988) 1379
- [7] P. L. Frabetti et al., PL B427 (1998) 211
- [8] S. Barlog et al., PL B233 (1989) 522
- [9] P. Coteus et al., PRL 59 (1987) 1530
- [10] S. F. Biagi et al., PL 150B (1985) 230
- [11] P. L. Frabetti et al., PRL 70 (1993) 2058
- [12] S. Barlog et al., PL B236 (1990) 495
- [13] M. I. Adamovich et al., PL B358 (1995) 151
- [14] P. L. Frabetti et al., PL B357 (1995) 678
- [15] N. Bondar et al., “E781 Beam Transition Radiation Detector” H-Note 746, SELEX Internal Report (1995)
- [16] A. Atamantchuck, SELEX Collaboration, “Design and Performance of the Fermilab E781 (SELEX) Hardware Scattering Trigger”, Nucl. Inst. Meth. A425 (1999) 529-535
- [17] P. Pogodin et al., “Drift chambers of the M1 spectrometer: The Detector, Electronics and Software”, H-Note 788, SELEX Internal Report (1997)

- [18] M. K. A. Antonov, G. Dsyubenko, “Geometry of Assembled E781 Photon 1, 2 Detectors”, H-Note 748, SELEX Internal Report (1997)
- [19] V. Maleev et al., “Description and test results for DPWC and TRD in E781”, H-Note 747, SELEX Internal Report (1995)
- [20] http://www.lns.cornell.edu/public/CLEO/soft/QQ/qq_expert.html
- [21] CMS Technical Design Report, CERN/LHCC 94-38
- [22] P. Gorodetzky, Rad. Phys and Chem. 41 (1993) 253
- [23] N. Akchurin et al.; Nucl. Inst. Meth. A379 (1996) 526-527
- [24] V.V. Abramov et.al., “Studies of the response of the prototype CMS hadron calorimeter, including magnetic field effects, to pion, electron, and muon beams”, CMS Note 2000/003
- [25] N. Akchurin et al., Nucl. Inst. Meth. A400 (1997) 267-278
- [26] N. Akchurin et al., Nucl. Inst. Meth. A399 (1997) 202-226
- [27] N. Akchurin et al., “PYTHIA-GEANT calculation of resolutions and reconstruction efficiencies in an Fe HF calorimeter”, CMS Note 2000-004
- [28] N. Akchurin et al., “The $\eta=3$ region of EE, HE and HF: using 1 TeV jets in PYTHIA-GEANT”, CMS-Note 2000-006
- [29] N. Akchurin et al., “Effects of channel-failure rates on the jet reconstruction efficiencies and resolutions in an Fe HF calorimeter”, CMS-Note 2000-005
- [30] N. Akchurin et al., Nucl. Inst. Meth. A409 (1998) 593-597
- [31] N. Akchurin et al., “Preliminary results from situ quartz fiber neutron radiations”, CMS-Note 1998-056

[32] F. Cogswell et al., “Measurements of 20 Hamamatsu R-5900 Photomultiplier Tubes for ATLAS TileCal Module-0”, ATLAS Internal Note TILE-CAL-NO-156 (1996)

[33] Y. Shao et al., Nucl. Inst. Meth. A454 (2000) 379-388

[34] Photomultiplier Tubes, Principles and Applications, PHILIPS

[35] Photomultiplier Tubes, Basics and Applications, HAMAMATSU